J. Fluid Mech. (2018), *vol.* 837, *pp.* 115–128.
doi:10.1017/jfm.2017.844

Gel-controlled droplet spreading

M. Jalaal[1,†], C. Seyfert[2], B. Stoeber[1,3] and N. J. Balmforth[4]

[1]Department of Mechanical Engineering, University of British Columbia, Vancouver, V6T 1Z4, BC, Canada

[2]Institute of Fluid Mechanics, Technical University of Dresden, 01069 Dresden, Germany

[3]Department of Electrical and Computer Engineering, University of British Columbia, Vancouver, V6T 1Z4, BC, Canada

[4]Department of Mathematics, University of British Columbia, Vancouver, V6T 1Z2, BC, Canada

(Received 3 January 2017; revised 13 October 2017; accepted 16 November 2017; first published online 19 December 2017)

Spreading and stationary droplets of a thermally responsive fluid on a heated surface are studied. The fluid undergoes a reversible gel formation at elevated temperature. The spatio-temporal pattern of gel formation within the droplet is examined using an experimental method based on spectral domain optical coherence tomography and time varying speckle patterns. Two stages of gel formation can be distinguished: first, a thin crust appears starting at the contact line. Second, a gel layer appears above the heated plate and then expands upward. We attribute the first stage of gel formation to solvent evaporation and heating through the air and the second to thermal conduction through the fluid from the base. Gel formation at the contact line is likely responsible for the arrest of spreading droplets, but was not detectable with our experimental protocol at the time of contact line arrest, suggesting that this arose over a microscopic length scale. Overall, substrate heating provides an effective way to control the final shape of droplets of thermo-responsive fluids.

Key words: complex fluids, drops, drops and bubbles

1. Introduction

Many industrial processes exploit the spreading of droplets of complex fluids over surfaces, such as coating (Ashmore *et al.* 2008), plant treatment with pesticides (Bergeron *et al.* 2000), inkjet printing (Basaran, Gao & Bhat 2013; Talbot *et al.* 2014) and three-dimensional printing of structured materials (Lewis 2006). In many of these applications, high precision over small spatial scales is required and it is vital that droplet spreading is not only fully understood but controllable. In order to optimize the droplet–surface interaction, different approaches have been developed, mostly involving the modification of either the fluid or the substrate. For the fluid, it is most common to change the rheology by using polymer additives (Bergeron *et al.* 2000; Smith & Bertola 2010), to introduce viscoelasticity (Cooper-White, Crooks & Boger 2002) or viscoplasticity (Saïdi, Martin & Magnin 2010). For the surface, the most popular approach is to modify the wetting properties (Josserand & Thoroddson 2016).

† Email address for correspondence: mazi@alumni.ubc.ca

Here, we use an aqueous solution of a thermo-responsive polymer (commercially available under the trade name Pluronic F127) that undergoes a reversible sol–gel transition at a certain temperature (Prud'homme, Wu & Schneider 1996) and has previously been used to actively or passively control flow in microchannels (Stoeber *et al.* 2005, 2006). It has previously been shown that droplet impact of Pluronic F127 can be controlled by heating the substrate (Jalaal & Stoeber 2014). To further understand the detailed mechanism underlying this control, here we conduct a new set of experiments in which we seek to visualize the formation of gel within the spreading droplet. The situation has many common points with studies of how solidification affects the spreading of molten droplets on cooled surfaces (Schiaffino & Sonin 1997*a*,*b*). Our thermo-responsive problem differs in that fluid is heated instead of cooled, gel formation requires significantly less heat than the latent heat for solidification of wax or metals (Wanka, Hoffmann & Ulbricht 1994), and the hydrogel is not a solid but a yield-stress fluid (Jalaal *et al.* 2017).

Our main experimental tool is a spectral domain optical coherence tomograph (SD-OCT). This interferometric device combines a broadband light source with a spectrometer to obtain depth images from the back-scattered light within the field of view (Drexler & Fujimoto 2008). SD-OCT images have been used previously to perform particle image velocimetry using tracer particles suspended in a fluid (Buchsbaum *et al.* 2015). Here, we use the device in a different fashion: by seeding the fluid with sub-micron-sized particles we may exploit the Brownian motion of these tracers to detect regions with elevated effective viscosity, and therefore the gel. In essence, this technique relies on collecting the interference signal resulting from the back scattered light from all particles within the local volume of fluid sampled by the SD-OCT, which changes over time as the positions of the particles change due to Brownian motion ('dynamic speckle'). This methodology is related to diffusing wave spectroscopy (Pine *et al.* 1988), differential dynamic microscopy (Cerbino & Trappe 2008), speckle variance optical coherence tomography (Mahmud *et al.* 2013) and some types of confocal microscopy (Bodiguel & Leng 2010), previously used for many applications from microrheology (Crocker & Grier 1996; Mason *et al.* 1997; Squires & Mason 2009) to the detection of microvascular networks (Conroy, DaCosta & Vitkin 2012). Counter to the previous techniques, our method identifies a region as being gelled when its speckle pattern does not change with time.

2. Experiments

2.1. *Pluronic F127*

For our experiments, we use a 16.3 wt% solution, prepared by dissolving Pluronic F127 powder (manufactured by BASF) in distilled water under gentle agitation at 4 °C for 24 h. At low temperature, the solution behaves as a Newtonian fluid; for higher temperatures, the material undergoes a transition to a gel and thereby inherits a yield-stress and rate-dependent plastic viscosity (Wanka *et al.* 1994; Jalaal *et al.* 2017). The gel temperature (defined as the temperature at which the material developed a detectable yield stress) decreases with the Pluronic F127 concentration as indicated by the data and fit shown in figure 1, taken from Jalaal *et al.* (2017).

To introduce tracers, we added 0.5 μm polystyrene beads (from Microspheres-nanospheres©) to the solution, to a concentration of 0.2 wt%. This concentration was too low to affect the rheology of the fluid which was determined using a rheometer. The density of the particles was slightly larger than water ($\sim$1040 kg m^{-3}), but not to the degree that buoyancy effects became important or that the density of the solution

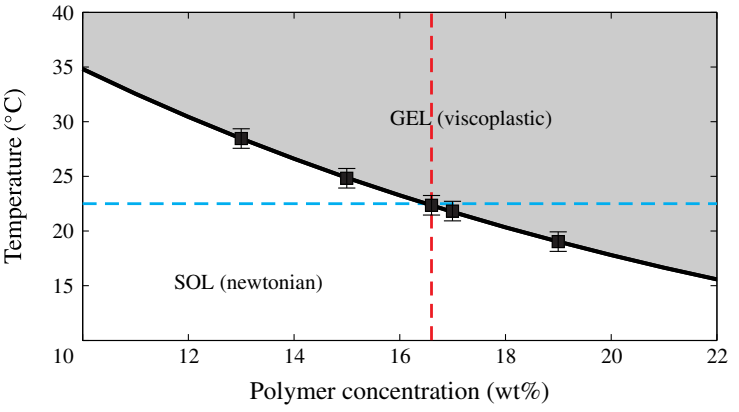

FIGURE 1. (Colour online) Phase diagram of aqueous solution of Pluronic F127. The points show experimental measurements and the solid black line shows the fit, $T_g = 68.1\,^{\circ}\mathrm{C}\,\exp(-0.068\mathcal{C})$, where $\mathcal{C}$ is the concentration of the polymer in wt% (Jalaal *et al.* 2017). The dashed lines indicate the initial polymer concentration and its gel temperature of the droplets used in this work.

was significantly modified. The final solution had a gel temperature of 22.5 °C (figure 1). The solution had thermal conductivities of 0.51 and 0.54 W (m K)$^{-1}$ in the sol and gel phases, respectively (measured using a C-Therm thermal conductivity analyzer). At temperatures well below the gel point, the solution had a viscosity of about 0.027 Pa s. The gel had a yield stress of $\tau_Y \approx 130$ Pa, flow index of $n \approx 0.42$ and consistency of $K \approx 12.5$ Pa s^n, as estimated from a Herschel–Bulkley fit to flow curve data from a rheometer. Note, this fit does not depend strongly on T.

2.2. *Experimental set-up*

The substrate for our droplet tests was a clean microscope coverslip (Thermo Scientific) of thickness 0.15 ± 0.02 mm enclosed within the apparatus sketched in figure 2. Instead of performing impact tests, we opted to conduct experiments with rather slower spreading droplets by extruding fluid just above the coverslips using a syringe pump (KD Scientific, Model Legato 111) fitted with 1 ml glass syringes and stainless steel needles with inner diameter 0.305 mm. Stiff tubing (polyurethane with wall thickness of 0.8 mm) was used to connect the syringe and the nozzle. The tip of the nozzle was located 0.55 mm above the substrate and a target volume was set as 0.02 ml. The flow rates of the extrusion varied from 0.01 ml min^{-1} to 0.15 ml min^{-1}. We also conducted a number of experiments with stationary droplets of the same target volume, deposited manually on the coverslips using a pipette.

The substrate was set above a heater inside an enclosure that shielded the experiment and maintained a steady ambient temperature and humidity. A solvent trap inside the enclosure kept the relative humidity at 94 ± 4 % (measured by a DHT22 humidity sensor), at least up until the heater was activated.

The heater was a 40 mm × 40 mm Peltier device with a nominal wattage of 60 W connected to a variable power supply. The applied heating protocol implemented an almost linear rate of increase in surface temperature, $\mathcal{T}_t$, varying from $\mathcal{T}_t = 0.07$ to 1.67 °C s^{-1}. A surface-mounted T-type thermocouple (from Omega) measured the substrate temperature. A glass sheet with a thickness 1 mm was placed between

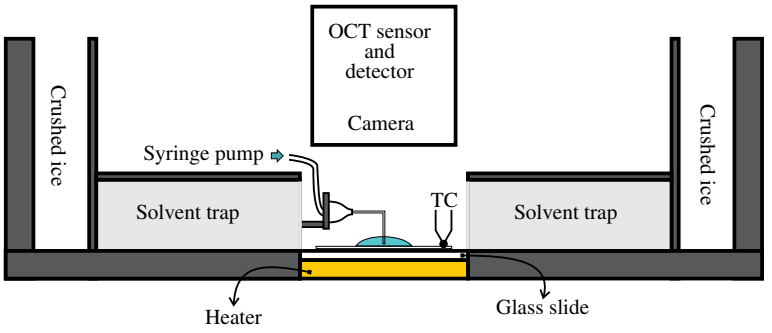

FIGURE 2. (Colour online) The experimental set-up for the investigations into the gel layer formation in Pluronic F127 droplets. Droplets were extruded on a thin cover slip placed above a heater. Images were captured from above using a CCD camera, while simultaneously conducting optical coherence tomography from the same angle. TC indicates the thermocouple used to measure the surface temperature.

the coverslip and the Peltier device to help make the heating more uniform at the base of the fluid. Thermal paste was used to enhance the heat transfer between the glass sheet and the Peltier device. Crushed ice packed into the walls of the enclosure established a steady temperature which was sufficiently below the gel temperature to ensure that the droplets were liquid at the beginning of each experiment.

2.3. *Imaging technique*

Within the solvent trap, the droplets were observed from above. The position of the contact line of the extruded droplets was measured directly using a CCD camera. However, our main tool was a SD-OCT instrument from Thorlabs (TEL1300V2-BU). This device uses broadband illumination, centred at a wavelength of 1300 nm, to perform cross-sectional scans through the target volume below the OCT with a beam width $\sim$13 μm. The maximum depth of the scan is approximately 3.5 mm, with an axial resolution of $\sim$4.2 μm. The horizontal extent of the cross-section has a resolution of $\sim$13 μm, corresponding to the beam width. The cross-sectional images were recorded with a rate of 5 per second.

A sample raw image from the OCT is shown in figure 3(*a*). The image shows a distortion due to refraction at the curved interface of the droplet. In order to correct for this, we mapped the apparent pixels to their true positions as follows: first, the interface of the droplet was identified employing an edge detection algorithm, and then fitted using a Fourier series ($f_{int}(x)$) in order to compute its slope. Provided the OCT scanning beam is vertical, the angles of incidence α and refraction β can then be determined:

$$\alpha = \tan^{-1}\left(\frac{\mathrm{d}f_{int}}{\mathrm{d}x}\right), \quad \beta = \sin^{-1}\left(\frac{n_{air}}{n_{liq}}\sin\alpha\right), \tag{2.1a,b}$$

where n_{air} and n_{liq} are the refractive indices of air and droplet, respectively. Hence,

$$x' = x - L_D\sin(\alpha-\beta), \quad y' = f_{int}(x) + L_D\cos(\alpha-\beta), \tag{2.2a,b}$$

where primed symbols note the mapped coordinates and $L_D = [\,y - f_{int}(x)]/n_{liq}$. Finally, the mapped image is linearly interpolated onto an equally spaced two-dimensional grid.

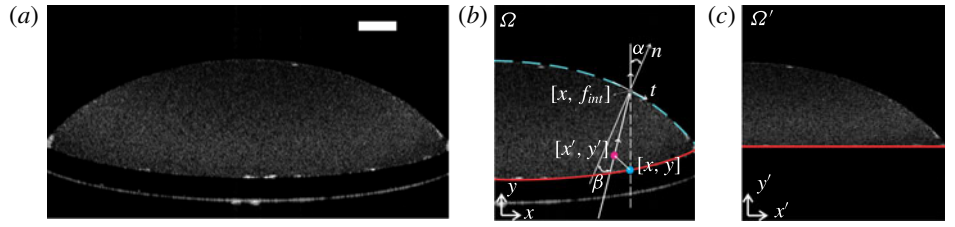

FIGURE 3. (Colour online) (*a*) An example of a raw OCT image and the mapping algorithm. In (*b*), the blue dashed line shows the droplet interface, f_{int}; α and β are the angles of incidence and refraction, respectively; $\boldsymbol{n}$ and $\boldsymbol{t}$ are the normal and tangential vectors at $[x, f_{int}]$. We map the pixels below the interface $[x, y]$ to their true positions $[x', y']$, using (2.2). The corrected image is shown in (*c*). The scale bar indicates 0.5 mm.

Note, in figure 3 and all the images we present later, the particles at the top of the droplet are slightly darker, but there is no change in their density. This occurs because the top of the droplet is slightly out of the focus of the SD-OCT system, and has no influence on the processing that we perform below to detect the decorrelating effect of Brownian motion.

2.4. *Detection of collective Brownian motion*

We identify gelled regions inside the droplet by exploiting the Brownian motion of the polystyrene beads. From the Stokes–Einstein relation (Squires & Mason 2009), the mean squared displacement of a Brownian particle over a time interval Δt, is

$$\langle x^2 \rangle = \frac{2k_B}{3\pi d}\frac{T}{\mu(\dot{\gamma}, T)}\Delta t, \tag{2.3}$$

where k_B is the Boltzmann's constant, d is the particle diameter and μ is the apparent dynamic viscosity, which is a function of the local shear rate $\dot{\gamma}$ and absolute temperature T. For $d = 0.5$ μm and the time frame $\Delta t = 0.2$ s used for the OCT image scans, equation (2.3) implies a displacement of $\sqrt{\langle x^2 \rangle} \sim O(0.1\ \mu\text{m})$, for the liquid Newtonian phase of the Pluronic solution. This displacement is much smaller than the spatial resolution of the OCT. Despite this, consecutive images of liquid-phase Pluronic solution seeded with a sufficient density of tracer particles show significant temporal variability in the absence of any apparent macroscopic fluid flow as a result of dynamic speckle, the time varying interference in the scattered light from multiple objects due to unresolved Brownian motion of the scatterers (Rabal & Braga 2008). By contrast, image pairs of particle-seeded Pluronic gel are identical except for minor fluctuations caused by noise. Evidently, the tracer particles are effectively immobilized in the gel due to a low-shear-rate effective viscosity that is orders of magnitude higher than that of the liquid phase. This sharp contrast between the degree of intensity fluctuation in the liquid and gel phases (see supplementary movie 1 available online at https://doi.org/10.1017/jfm.2017.844) provides the means to detect the gelled regions in droplets of Pluronic. Dynamic speckle arises provided there are multiple scatter sources within each volumetric region contributing signal to a volume element (voxel) recorded by the SD-OCT. For the OCT, this volumetric region is about 845 μm^3, and we found that concentrations above 0.1 wt% provided a sufficient number of particles per voxel $\mathcal{N}_p$ to register the speckle effect. The concentration $c = 0.2$ wt% used in the droplet experiments corresponds to $\mathcal{N}_p \approx 26$.

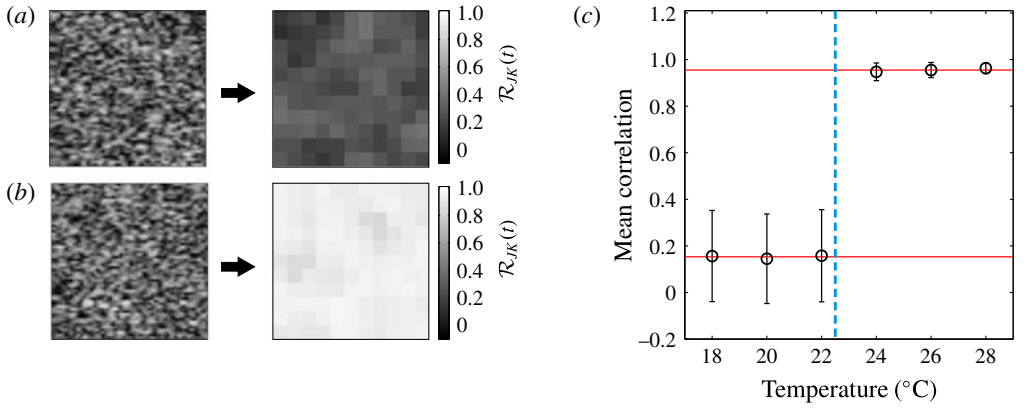

FIGURE 4. (Colour online) Raw image and corresponding correlation map of Pluronic F127 seeded with $d = 0.5$ μm particles to a concentration of 0.2 wt%, over a 510 × 510 μm^2 square at (*a*) 18 °C. (*b*) 28 °C. (*c*) Variation of average correlation value with temperature. The horizontal lines show the average values for sol and gel phases. The dashed line indicates the gel temperature T_g (figure 1).

2.5. *Quantification of Brownian motion*

We quantify the fluctuation of the intensity signal as follows. Let $I_{jk}(t = n\Delta t)$ denote the measured intensity of the (j, k)th pixel in the nth image, of which there are N altogether $(n = 1, 2, \ldots, N)$. We then coarse grain the image area into M interrogation windows of a given edge length (about 42 μm), and then compute the correlation coefficient, $R_{JK}(t)$, between consecutive images for the (J, K)th window. To help reduce the effect of noise, we then formulate the three-point running average,

$$\mathcal{R}_{JK}(t) = \tfrac{1}{3}[R_{JK}(t - \Delta t) + R_{JK}(t) + R_{JK}(t + \Delta t)]. \tag{2.4}$$

If consecutive images are identical, then $\mathcal{R}_{JK}(t) = 1$. Small values of $\mathcal{R}_{JK}$ imply little relation between those images.

We first image stationary drops of the thermo-responsive solution seeded with the polystyrene beads. The temperature of the liquid was changed from 18 to 28 °C and cross-sectional scans of size ∼510 × 510 μm^2 (and thickness 13 μm), at the centre of the droplet, were taken over durations of 4 s (20 images). Examples of raw images and their corresponding correlation maps for sol and gel phases are illustrated in figure 4(*a*,*b*). Figure 4(*c*) shows mean correlation values against temperature, taking the average over both time and all the interrogation windows in the image. The fluctuations in the positions of the suspended particles for the liquid phase are relatively large, leading to a low average correlation (less than 0.2). Elevating the temperature above T_g, the Brownian motion of the particles is significantly reduced to a degree where the correlation reaches values exceeding 0.9. We therefore adopt $\mathcal{R}_{JK} > 0.75$ as a convenient threshold to detect the gel in spreading droplets. The results were insensitive to the precise choice of the threshold provided that $0.55 < \mathcal{R}_{JK} < 0.8$.

3. Results

3.1. *Gel formation patterns in stationary droplets*

This section outlines our visualization of gel formation inside droplets of Pluronic solution. We start the investigation with a relatively simple situation, that of a sessile

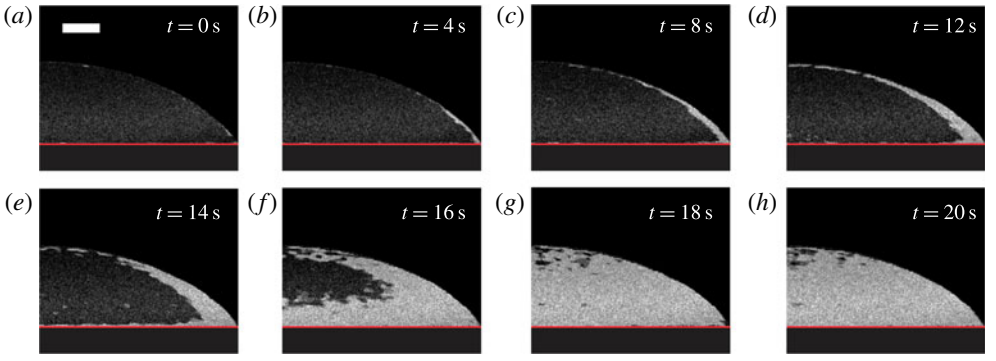

FIGURE 5. (Colour online) Gel formation in a stationary droplet on a heated substrate. Shown are snapshots of the droplet at the times indicated. The brightened areas indicate the interrogation windows where the correlation $\mathcal{R}_{JK}$ exceeds the threshold 0.75. The heating rate was $\mathcal{T}_t \approx 0.70\,^{\circ}\mathrm{C\ s^{-1}}$. Half of the droplet is shown and the scale bar indicates 0.5 mm.

droplet. Figure 5 shows sample gel formation patterns induced by heating the surface underneath the droplet. Shown are snapshots of the droplet after the removal of image distortion, with the underlying surface indicated. The brightened areas superimposed on the snapshots indicate the interrogation windows where the correlation $\mathcal{R}_{JK}$ exceeds the 0.75 threshold.

From figure 5, two stages of gel propagation can be distinguished: the first stage corresponds to the creation of a superficial crust near the outer rim of the droplet. The crust first appears at the contact line, then advances along the surface and thickens with time. In the second stage of gel formation, which is initiated somewhat later, a growing layer appears above the heated plate and then expands upwards. Figure 6, shows the changes in the thickness of the gel layers in the two stages over time; H_{crust} denotes the thickness of the surface gel layer just above the substrate (close to the contact line) and H_{base} is the thickness of the gel layer growing from the base at the centre of the droplet. As seen in figure 5, the crust forms well ahead of the moment at which the substrate reaches the gel temperature; the second stage, however, starts after that moment. Our interpretation of the phenomenology seen in figure 5 is that the droplet is heated in two different ways. First, because heat can be transferred through air by diffusion or convection more quickly than in the Pluronic solution, the air surrounding the droplet heats up faster than the fluid above the plate (cf. Dunn *et al.* 2009; Ait Saada, Chikh & Tadrist 2010; Sáenz *et al.* 2015). By itself, this cannot explain the formation of a gelled crust below the gel temperature. However, the heating of the air also changes the relative humidity, prompting evaporation from the droplet interface, which increases the local polymer concentration and therefore lowers the gel temperature. Thus, we attribute the first stage of gel formation to a combination of interface heating and evaporation. Dimensional analysis in support of this conclusion is presented in appendix A. The second wave of gel formation is simply the result of heat conduction directly through the base of the droplet. Note, because of evaporation, one should expect a change in the volume of the droplet. Also, a weak evaporation driven flow might occur. Both of these are found to be negligible, for the time scales of our problem. In fact, in other experiments (not shown here), we also visualized the flow inside the stationary droplet, observing no significant internal convection.

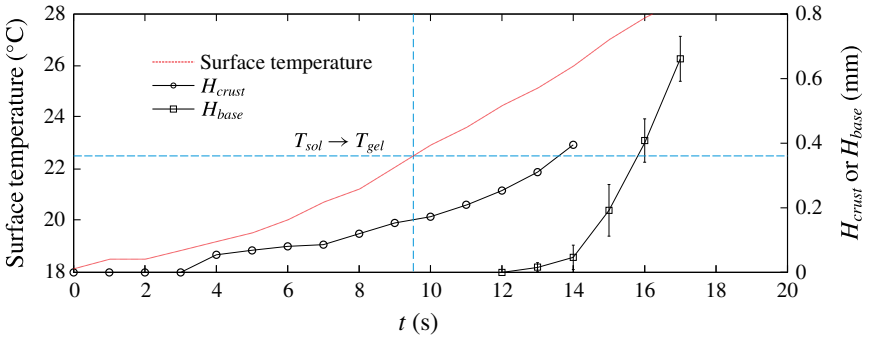

FIGURE 6. (Colour online) Temperature of the coverslip and the thickness of the gel layer just above the substrate and at the centre of the droplet (denoted H_{crust} and H_{base}, respectively) over time for the heated stationary droplet shown in figure 5. H_{crust} is measured perpendicularly to the surface and by following the crust layer and extrapolating to the base. The error bars indicate the uncertainty of identifying the location of the gel–liquid interface from images as in figure 5.

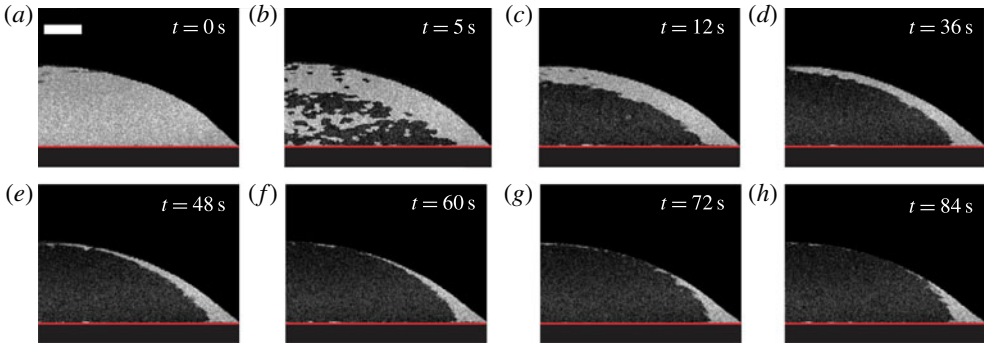

FIGURE 7. (Colour online) Liquefication of an initially gelled droplet (the brightened regions identify interrogation windows over which $\mathcal{R}_{JK} > 0.75$). The initial temperature was 40 °C. The scale bar indicates 0.5 mm.

We also found it instructive to examine the spatio-temporal pattern characterizing how gel disappeared and the droplet liquefied after the heater was turned off and the temperature fell below T_g. Figure 7 shows such a cooling sequence, where the heater was turned off 5 s after the whole droplet was gelled up. As the temperature falls, gel disappears abruptly from the bulk of the droplet. However, a persistent crust remains near the rim over times far longer than the experiment. We attribute this crust to the enhanced evaporation that assists the first wave of gel formation; when the drop is subsequently cooled, the gel temperature of the crust is lower than that of the bulk of the droplet, and this region only liquefies at a later time. Indeed, the evaporation is evidently sufficient to leave a concentrated gelled crust near the contact line at the end of the experiment. This effect likely disappears if the hot fluid stopped evaporating and was able to reach phase equilibrium through diffusion, erasing any memory of its thermal history.

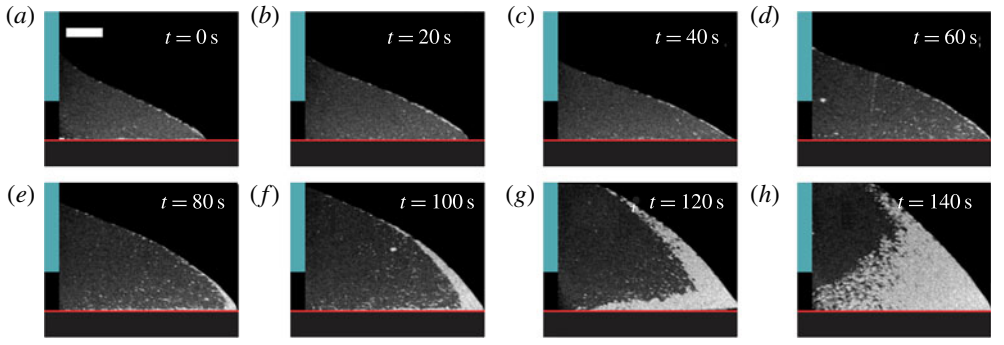

FIGURE 8. (Colour online) Spreading and solidification of a Pluronic F127 droplet with a target volume of 20 μl on a heated substrate. The flow rate was 10 μl min^{-1} and $\mathcal{T}_t = 0.074\,^{\circ}\text{C}\ \text{s}^{-1}$. The vertical bar indicates the location of the nozzle. Only half of the droplet is shown and the white horizontal bar has length 0.5 mm.

3.2. *Gel formation in spreading droplets*

The phenomenology of gel formation in the tests performed by extruding droplets from the nozzle attached to the syringe pump (§ 2.2 and figure 2) was similar to that for stationary droplets; figure 8 shows a sample sequence of processed SD-OCT pictures. The droplet is extruded with a flow rate of 10 μl min^{-1} and a $\mathcal{T}_t$ of $0.074\,^{\circ}\text{C}\ \text{s}^{-1}$, and spreads axisymmetrically. In this particular experiment a relatively low heating rate $\mathcal{T}_t$ was applied in order to make the gel formation clearly detectable, and the heater turned on at the same time as the pump.

At the beginning of the extrusion, the droplet grows and wets the surface without noticeable gel formation. At a certain moment, this spreading ceases when the contact line becomes pinned at a radius significantly smaller than the final radius of an isothermal extrusion. After the pinning, the continued extrusion of fluid deepens the droplet and raises the apparent contact angle. During the pinning process, no gel could be detected. Only once the contact line was brought to a halt could one detect the first wave of gel formation in the superficial crust, followed by the second wave propagating from the base. The most notable difference between the stationary and extruding droplets was the behaviour underneath and close to the nozzle, where the continued extrusion precluded the formation of static gel regions and continually deepened the droplet.

Gel cannot therefore be detected at the moment that the contact line becomes pinned. Evidently, no extensive layer of gelled-up material at the base is needed for this arrest. Nor does the correlation $\mathcal{R}_{JK}$ obviously decrease throughout the bulk of the droplet, ruling out a rise in bulk viscosity. Our results are not therefore consistent with the theory of Schiaffino & Sonin (1997*b*), which ignores any heating effect of the surrounding air. Instead, we conjecture that gel structure at an undetectable spatial scale forms first at the contact line and is sufficient to arrest the spreading of the droplet (cf. Tavakoli, Davis & Kavehpour 2014), modulo the effect of any apparent slip (Qian, Park & Breuer 2015).

3.3. *Gel-controlled spreading*

Figure 9 plots the final radii of droplets as a function of the flow rate Q of the syringe pump for a suite of experiments with and without surface heating (panel *a*) and for

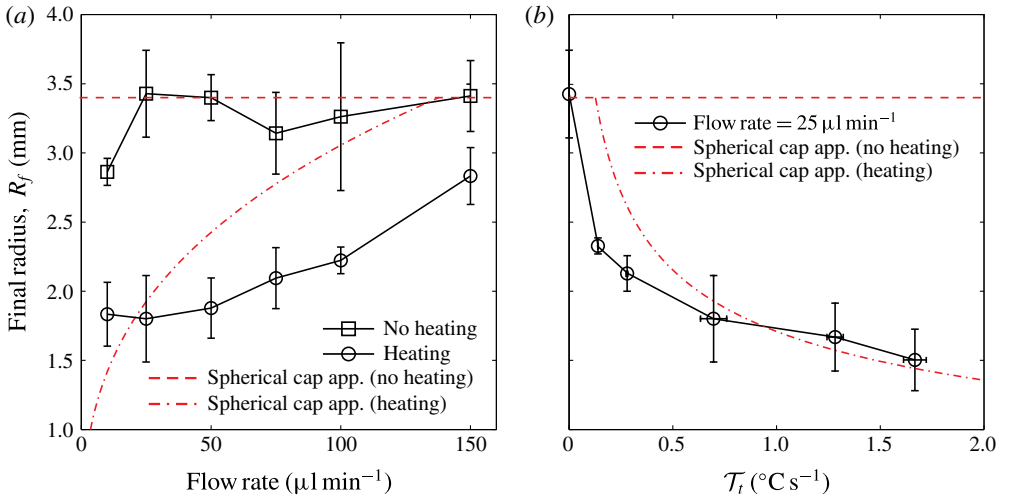

FIGURE 9. (Colour online) Final radii of Pluronic droplets extruded with (*a*) different flow rate and a constant heating rate of $\mathcal{T}_t = 0.70\,^{\circ}\mathrm{C\ s^{-1}}$, and (*b*) varying heating rate and constant flow rate of 25 μl min^{-1}. The final target volume in all experiments was 0.02 ml. In panel (*a*), the squares show corresponding results without surface heating and the dashed line shows the radius expected for a spherical cap of the same volume and a contact angle of 35°.

different heating rates $\mathcal{T}_t$, all with the same target volume (panel *b*). The data points in figure 9 indicate the average final radius and the error bars indicate the standard deviations over five different experiments. Without surface heating, the droplets spread to a final radius that does not depend on the flow rate. With surface heating, however, the spread of the droplet is arrested at a radius that decreases as the flow rate Q is reduced or as the heating rate $\mathcal{T}_t$ is increased.

Throughout the experiments without surface heating (or small $\mathcal{T}_t$), it was common to get asymmetric shapes of droplets. The liquid would randomly stop and 'stick' for a moment and then suddenly spread further in the same or different direction for no obvious reasons. This behaviour, which may well reflect the effect of surface inhomogeneities, generates the relatively large standard deviations in the radius measurements in figure 9(*a*). Asymmetric pinning did not occur for higher heating rates, with droplets remaining axisymmetrical (as in figure 8), and for the most part appeared to trigger irregular variations in the gel-induced arrest of the contact line rather than preventing it.

For the target volume used in figure 9, the final radius corresponded to the location where the contact line first became pinned. In larger volume extrusions, this was not always the case: deepening droplets with arrested contact lines could breach the gel dams at their peripheries over certain angular locations to lead to further, non-axisymmetrical spreading events at later times. In such high volume experiments, the contact line therefore advanced in an episodic and spatially irregular manner. Though interesting, we avoid further consideration of such cases here.

To offer a simple theoretical counterpart to figure 9, we assume that the extrusion proceeds sufficiently slowly over the liquid phase that the droplet marches through a series of (spherical cap) equilibria set by a contact angle θ and the instantaneous

volume, $V(t)$, at time t. The radius, $R(t)$, is then

$$R(t) = \left[\frac{3V(t)\sin^3\theta}{(2+\cos\theta)(1-\cos\theta)^2}\right]^{1/3}. \tag{3.1}$$

For a target volume of $V_f = 0.2$ µl and a contact angle of $\theta = 35°$, this predicts a final radius R_f of 3.4 mm for an extrusion without surface heating, as also shown in figure 9(*a*). If we assume that the contact line pins when the plate reaches the gel temperature T_g, then this must occurs at time $t_g = (T_g - T_0)/\dot{T}_t$ after heating is commenced, where T_0 denotes the initial temperature. The volume at the moment of arrest is $V_g = Qt_g$. Hence,

$$R_f(Q, \dot{T}_t) = \left[\frac{3Qt_g\sin^3\theta}{(2+\cos\theta)(1-\cos\theta)^2}\right]^{1/3}, \tag{3.2}$$

provided the gel temperature is reached during the extrusion.

The prediction in (3.2) is compared with experimental results in figure 9, and noticeably overpredicts the final radii of the experimental droplets, in particular when the heating rate is small or the flow rate is high. This discrepancy is not surprising in view of the omission of evaporation in arriving at (3.2), an effect critical to the development of a superficial crust and the arrest of the contact line below the expected gel temperature. The influence of the heating rate on the final radius, and therefore the potential to control the degree of spreading, is highlighted in figure 9(*b*); higher heating rates lead to smaller final radii.

4. Conclusions

In this paper, we have studied experimentally the spreading of droplets of thermo-responsive fluid over a heated solid surface. The yield stress of the gelled solution furnishes a means to externally control the final radius. Using optical coherence tomography (OCT) we detected the spatio-temporal patterns characterizing the evolving regions of gel in spreading and stationary droplets. This observational method exploits the temporal varying speckle patterns that appear when the material is seeded with a sufficiently high concentration of scattering particles. The results indicate that gel first forms a thickening superficial crust near the contact line, due to a combination of evaporation and heating by the surrounding air. Somewhat later, heat conduction through the base leads to a gel layer that expands rapidly upwards through the bulk of the droplet. Despite this, we were not able to directly observe how the contact line became pinned, and conjecture that the formation of microscopic amounts of gel in its vicinity are responsible.

The OCT provides cross-sectional images of fluids flow at small scales. In comparison with common confocal imaging systems, OCT is faster and does not require the stack of multiple planar images to construct the cross-sectional picture (cf. Wereley & Meinhart 2010). Additionally, by observing the Brownian motion of particles, one can distinguish regions with low and high apparent viscosities, providing a unique experimental method to visualize the *in situ* phase change in fluids. This can be used for several fluid mechanics applications, from skin formation (cf. Arai & Doi 2012) and sol–gel transition (cf. Talbot *et al.* 2014) in droplet evaporation to crystal formation in fluids (cf. Bhola & Chandra 1999).

Acknowledgements

M.J. acknowledges the support of Natural Sciences and Engineering Research Council of Canada through a Vanier Canada Graduate Scholarship. The authors thank F. Foroughi, M. Leitner, S. Odenbach, A. Marin and M. Martinez for the useful discussions. This research was undertaken, in part, thanks to funding from the Canada Research Chairs program.

Supplementary movie

Supplementary movie is available at https://doi.org/10.1017/jfm.2017.844.

Appendix A

The Hertz–Knudsen relation (Prosperetti & Plesset 1984; Sultan, Boudaoud & Amar 2005) connects the mass flux at the interface Γ to the local change in vapour density ρ_v, which arises here due to a temperature change ΔT:

$$\Gamma \approx v_{th} \left[\frac{\mathrm{d}\rho_v}{\mathrm{d}T}\right]_{T=T_i} \Delta T. \tag{A 1}$$

Here, T_i is the initial air temperature and $v_{th} = \alpha\sqrt{k_B T_i/(2\pi M)}$ is a kinetic velocity, defined in terms of an accommodation coefficient $\alpha \sim 1$, the Boltzmann constant k_B, and the molecular weight of the vapour M. For water, $\mathrm{d}\rho_v/\mathrm{d}T \approx 10^{-3}$ kg (m^3 K)$^{-1}$ and $v_{th} \approx 150$ m s^{-1} (Sultan *et al.* 2005). Thus, $\Gamma \sim O(0.1)$ kg m^{-2} s for a temperature change ΔT of a few degrees.

In figure 6, the crust starts to appear after about 4 s, when the surface temperature is at 19 °C. From the phase diagram of the material (figure 1), gel formation at this surface temperature requires a polymer concentration of approximately 19 wt%, instead of the original 16 wt%. From the images, the skin layer at $t = 4$ s is observed from the video frames to have thickness $\delta \sim 0.1$ mm (figures 5 and 6). This is consistent with diffusive transport of water molecules over the skin, for which $\delta \approx \sqrt{\kappa t}$, if the diffusivity in the polymer solution is close to its value for pure water, $\kappa \sim 2 \times 10^{-9}$ m^2 s^{-1}, at the temperatures of the experiment. Moreover, to deplete a 0.1 mm thick skin layer by at least 3 wt% of its water content, one requires an evaporative mass flux greater than $\Gamma \approx 0.03\rho_s\delta/t \sim O(0.001)$ kg m^{-2} s, which is comfortably smaller than that predicted by the Hertz–Knudsen relation. Evaporation due to the change in vapour saturation density can therefore easily account for the drop in gel temperature. However, one should note that the evaporation rate may drop with time due to the increase in ambient humidity and the reduced diffusivity of water through the gel.

REFERENCES

Ait Saada, M., Chikh, S. & Tadrist, L. 2010 Numerical investigation of heat and mass transfer of an evaporating sessile drop on a horizontal surface. *Phys. Fluids* **22** (11), 112115.

Arai, S. & Doi, M. 2012 Skin formation and bubble growth during drying process of polymer solution. *Eur. Phys. J.* E **35** (7), 1–9.

Ashmore, J., Shen, A. Q., Kavehpour, H. P., Stone, H. A. & McKinley, G. H. 2008 Coating flows of non-Newtonian fluids: weakly and strongly elastic limits. *J. Engng Maths* **60** (1), 17–41.

BASARAN, O. A., GAO, H. & BHAT, P. P. 2013 Nonstandard inkjets. *Annu. Rev. Fluid Mech.* **45**, 85–113.

BERGERON, V., BONN, D., MARTIN, J. Y. & VOVELLE, L. 2000 Controlling droplet deposition with polymer additives. *Nature* **405**, 772–775.

BHOLA, R. & CHANDRA, S. 1999 Parameters controlling solidification of molten wax droplets falling on a solid surface. *J. Mater. Sci.* **34** (19), 4883–4894.

BODIGUEL, H. & LENG, J. 2010 Imaging the drying of a colloidal suspension. *Soft Matt.* **6** (21), 5451–5460.

BUCHSBAUM, A., EGGER, M., BURZIC, I., KOEPPLMAYR, T., AIGNER, M., MIETHLINGER, J. & LEITNER, M. 2015 Optical coherence tomography based particle image velocimetry (oct-piv) of polymer flows. *Opt. Laser Engng* **69**, 40–48.

CERBINO, R. & TRAPPE, V. 2008 Differential dynamic microscopy: probing wave vector dependent dynamics with a microscope. *Phys. Rev. Lett.* **100** (18), 188102.

CONROY, L., DACOSTA, R. S. & VITKIN, I. A. 2012 Quantifying tissue microvasculature with speckle variance optical coherence tomography. *Opt. Lett.* **37** (15), 3180–3182.

COOPER-WHITE, J. J., CROOKS, R. C. & BOGER, D. V. 2002 A drop impact study of worm-like viscoelastic surfactant solutions. *Colloids Surf.* A **210**, 105–123.

CROCKER, J. C. & GRIER, D. G. 1996 Methods of digital video microscopy for colloidal studies. *J. Colloid Interface Sci.* **179** (1), 298–310.

DREXLER, W. & FUJIMOTO, J. G. 2008 *Optical Coherence Tomography: Technology and Applications*. Springer Science & Business Media.

DUNN, G. J., WILSON, S. K., DUFFY, B. R., DAVID, S. & SEFIANE, K. 2009 The strong influence of substrate conductivity on droplet evaporation. *J. Fluid Mech.* **623**, 329–351.

JALAAL, M., COTTRELL, G., BALMFORTH, N. J. & STOEBER, B. 2017 On the rheology of pluronic f127 aqueous solutions. *J. Rheol.* **61** (1), 139–146.

JALAAL, M. & STOEBER, B. 2014 Controlled spreading of thermo-responsive droplets. *Soft Matt.* **10**, 808–812.

JOSSERAND, C. & THORODDSON, S. T. 2016 Drop impact on a solid surface. *Annu. Rev. Fluid Mech.* **48**, 365–391.

LEWIS, J. A. 2006 Direct ink writing of 3d functional materials. *Adv. Funct. Mater.* **16** (17), 2193–2204.

MAHMUD, M. S., CADOTTE, D. W., VUONG, B., SUN, C., LUK, T. W. H., MARIAMPILLAI, A. & YANG, V. X. D. 2013 Review of speckle and phase variance optical coherence tomography to visualize microvascular networks. *J. Biomed. Opt.* **18** (5), 050901.

MASON, T. G., GANESAN, K., VAN ZANTEN, J. H., WIRTZ, D. & KUO, S. C. 1997 Particle tracking microrheology of complex fluids. *Phys. Rev. Lett.* **79** (17), 3282–3285.

PINE, D. J., WEITZ, D. A., CHAIKIN, P. M. & HERBOLZHEIMER, E. 1988 Diffusing wave spectroscopy. *Phys. Rev. Lett.* **60** (12), 1134.

PROSPERETTI, A. & PLESSET, M. S. 1984 The stability of an evaporating liquid surface. *Phys. Fluids* **27** (7), 1590–1602.

PRUD'HOMME, R. K., WU, G. & SCHNEIDER, D. K. 1996 Structure and rheology studies of poly(oxyethylene-oxypropylene-oxyethylene) aqueous solution. *Langmuir* **12**, 4651–4659.

QIAN, B., PARK, J. & BREUER, K. S. 2015 Large apparent slip at a moving contact line. *Phys. Fluids* **27** (9), 091703.

RABAL, H. J. & BRAGA, R. A. 2008 *Dynamic Laser Speckle and Applications*. CRC Press.

SÁENZ, P. J., SEFIANE, K., KIM, J., MATAR, O. K. & VALLURI, P. 2015 Evaporation of sessile drops: a three-dimensional approach. *J. Fluid Mech.* **772**, 705–739.

SAÏDI, A., MARTIN, C. & MAGNIN, A. 2010 Influence of yield stress on the fluid droplet impact control. *J. Non-Newtonian Fluid Mech.* **165** (11), 596–606.

SCHIAFFINO, S. & SONIN, A. A. 1997*a* Formation and stability of liquid and molten beads on a solid surface. *J. Fluid Mech.* **343**, 95–110.

SCHIAFFINO, S. & SONIN, A. A. 1997*b* On the theory for the arrest of an advancing molten contact line on a cold solid of the same material. *Phys. Fluids* **9** (8), 2227–2233.

SMITH, M. I. & BERTOLA, V. 2010 Effect of polymer additives on the wetting of impacting droplets. *Phys. Rev. Lett.* **104**, 1–4.

SQUIRES, T. M. & MASON, T. G. 2009 Fluid mechanics of microrheology. *Annu. Rev. Fluid Mech.* **42** (1), 413–438.

STOEBER, B., HU, C.-M. J., LIEPMANN, D. & MULLER, S. J. 2006 Passive flow control in microdevices using thermally responsive polymer solutions. *Phys. Fluids* **18**, 053103.

STOEBER, B., YANG, Z., LIEPMANN, D. & MULLER, S. J. 2005 Flow control in microdevices using thermally responsive triblock copolymers. *J. Microelectromech. Syst.* **14**, 207–213.

SULTAN, E., BOUDAOUD, A. & AMAR, M. B. 2005 Evaporation of a thin film: diffusion of the vapour and Marangoni instabilities. *J. Fluid Mech.* **543**, 183–202.

TALBOT, E. L., YANG, L., BERSON, A. & BAIN, C. D. 2014 Control of the particle distribution in inkjet printing through an evaporation-driven sol–gel transition. *ACS Appl. Mater. Interfaces* **6** (12), 9572–9583.

TAVAKOLI, F., DAVIS, S. H. & KAVEHPOUR, H. P. 2014 Spreading and arrest of a molten liquid on cold substrates. *Langmuir* **30** (34), 10151–10155.

WANKA, G., HOFFMANN, H. & ULBRICHT, W. 1994 Phase diagrams and aggregation behavior of poly(oxyethylene)-poly(oxypropylene)-poly(oxyethylene) triblock copolymers in aqueous solutions. *Macromolecules* **27**, 4145–4159.

WERELEY, S. T. & MEINHART, C. D. 2010 Recent advances in micro-particle image velocimetry. *Annu. Rev. Fluid Mech.* **42**, 557–576.